

1           **Evaluating Radio Occultation (RO) Constellation**  
2           **Designs Using Observing System Simulation**  
3           **Experiments (OSSEs) for Ionospheric Specification**

4           **Nicholas Dietrich<sup>1</sup>, Tomoko Matsuo<sup>1</sup>, Chi-Yen Lin<sup>2</sup>, Brandon diLorenzo<sup>1</sup>,**  
5           **Charles Chien-Hung Lin<sup>3</sup>, Tzu-Wei Fang<sup>4</sup>**

6           <sup>1</sup>Ann and H.J. Smead Aerospace Engineering Sciences, University of Colorado Boulder, Boulder, CO

7           <sup>2</sup>Center for Astronautical Physics and Engineering, National Central University, Taoyuan, Taiwan

8           <sup>3</sup>Department of Earth Sciences, National Cheng Kung University, Tainan, Taiwan

9           <sup>4</sup>Space Weather Prediction Center, National Oceanic and Atmospheric Administration, Boulder, CO

10           **Key Points:**

- 11           • OSSE study assessing hypothetical RO constellations, the first to comprehensively  
12           account for forecast model and Abel inversion errors.
- 13           • The RO constellation with low- and high-inclination orbits at 520 km altitude per-  
14           forms the best with the highest observation counts.
- 15           • Uncharacterized Abel inversion errors and poorly retrieved low plasma density limit  
16           assimilation impact on the equatorial ionosphere.

---

Corresponding author: Nicholas Dietrich, [Nicholas.Dietrich@colorado.edu](mailto:Nicholas.Dietrich@colorado.edu)

**Abstract**

Low Earth orbit (LEO) radio occultation (RO) constellations can provide global electron density profiles (EDPs) to better specify and forecast the ionosphere-thermosphere (I-T) system. To inform future RO constellation design, this study uses comprehensive Observing System Simulation Experiments (OSSEs) to assess the ionospheric specification impact of assimilating synthetic EDPs into a coupled I-T model. These OSSEs use 10 different sets of RO constellation configurations containing 6 or 12 LEO satellites with base orbit parameter combinations of 520 km or 800 km altitude, and 24 degrees or 72 degrees inclination. The OSSEs are performed using the Ensemble Adjustment Kalman Filter implemented in the Data Assimilation Research Testbed and the Thermosphere-Ionosphere-Electrodynamics General Circulation Model (TIEGCM). A different I-T model is used for the nature run, the Whole Atmosphere Model-Ionosphere Plasmasphere Electrodynamics (WAM-IPE), to simulate the period of interest is the St. Patrick's Day storm on March 13-18, 2015. Errors from models and EDP retrieval are realistically accounted for in this study through distinct I-T models and by retrieving synthetic EDPs through an extension Abel inversion algorithm. OSSE assessment, using multiple metrics, finds that greater EDP spatial coverage leading to improved specification at altitudes 300 km and above, with the 520 km altitude constellations performing best due to yielding the highest observation counts. A potential performance limit is suggested with two 6-satellite constellations. Lastly, close examination of Abel inversion error impacts highlights major EDP limitations at altitudes below 200 km and dayside equatorial regions with large horizontal gradients and low electron density magnitudes.

**Plain Language Summary**

The upper atmosphere, the region above 100 km altitude, is strongly influenced by space weather events that can negatively impact ground and space-based technologies. These technologies include communication and navigation systems impacted by radio wave propagation through high altitudes plasma, a region called the ionosphere. Developing observing systems that provide global monitoring of the ionosphere is a critical need for understanding and forecasting space weather changes, such as radio occultations (RO) that provide plasma observations using global positioning radio signals. In this study, we evaluate these hypothetical RO observing systems in simulated experiments using data assimilation, an approach that integrates synthetic observations into a physics-based model. We find that increased observational coverage corresponds to better estimated plasma states, and that lower orbit altitude constellations yield higher observation counts. This study comprehensively incorporates model and observation errors to more realistically represent real-world conditions. One limitation of RO data is highlighted in regions near the equator and at lower altitudes (below 250 km) where there is a breakdown in assumptions for observation retrieval. This study illustrates the clear operational benefits of these plasma observations, informing the future observing system design and aiding their use for space weather forecasting.

**1 Introduction**

Monitoring the near-Earth space environmental conditions for space weather nowcasting and forecasting is increasingly pertinent to maintaining critical ground and space-based technological systems. One such critical impact is ionospheric plasma disturbances affecting navigational systems via the propagation of radio waves for Global Navigation Satellite Systems (GNSS) and very low frequency signals, along with other communication systems utilizing high frequency and ultra high frequency radio signals. The peak heights and magnitudes of plasma density affects whether radio signals are reflected or absorbed, the index of refraction that bends these signals, and small-scale plasma density irregularities can cause radio signals to scatter or scintillate. These space weather

67 effects on radio signals can be characterized using parameters, such as the F-region peak  
 68 electron density,  $N_mF_2$ , and its height,  $h_mF_2$ , the total electron content (TEC), the rate  
 69 of change of TEC index (ROTI), and the  $S_4$  index. Geomagnetic storms can induce con-  
 70 siderable variations and disturbances of the near-Earth plasma environments, stressing  
 71 our radio-based systems as indicated by dramatic changes in ROTI and  $S_4$  index (Moreno  
 72 et al., 2011). As underscored by the Promoting Research and Observations of Space Weather  
 73 to Improve the Forecasting of Tomorrow (PROSWIFT) Act in 2020 (Lugaz, 2020) and  
 74 space weather gap analysis findings (Vourlidis et al., 2023), continuing and developing  
 75 new ionospheric observing systems, as well as their integration into forecast models with  
 76 the help of data assimilation (DA), is essential for advancing space weather now-casting  
 77 and forecasting capabilities. Moreover, the Weather Research and Innovation Forecast-  
 78 ing Act of 2017 specifically mandates the National Oceanic and Atmospheric Associa-  
 79 tion (NOAA) to perform Observing System Simulation Experiments (OSSEs), wherein  
 80 DA frameworks are used to quantitatively assess hypothetical observing systems for their  
 81 relative value and benefit.

82 GNSS constellations are designed for global positioning, enabling radio occultation  
 83 (RO) observations with global coverage of the ionosphere. Currently available GNSS con-  
 84 stellations include GPS, GLONASS, Galileo, and BeiDou. The development and oper-  
 85 ation of RO satellite constellations have considerably grown over recent decades, pro-  
 86 viding real-time observations for ionospheric space weather prediction, climatological study,  
 87 and insight into ionospheric physics. In addition to their well-recognized and valuable  
 88 role as an observing system for ionospheric plasma density, recent DA studies (Matsuo  
 89 & Hsu, 2021; Dietrich et al., 2022) suggest their utility as a global monitoring system  
 90 of thermospheric mass density. Earth-based RO constellations began in 1995 with the  
 91 launch of MicroLab-1 Global Positioning System/Meteorology (GPS/MET) (Hajj & Ro-  
 92 mans, 1998; Kursinski et al., 1997), and was succeeded in 2006 by the FORMOSAT-3/COSMIC  
 93 (F3/C) (Anthes et al., 2008) and its follow-on mission FORMOSAT-7/COSMIC-2 (F7/C2)  
 94 (Yue, Schreiner, Pedatella, et al., 2014; Fong et al., 2019) in 2019. F3/C consisted of a  
 95 6-satellite low Earth orbit (LEO) constellation, orbiting in separate orbital planes, each  
 96 at  $72^\circ$  latitude and 800 km altitude. RO observations counts of F3/C were doubled with  
 97 the launch of the more recent F7/C2, a 6-satellite constellation in a similar orbit con-  
 98 figuration at  $24^\circ$  inclination and 550 km altitude. Commercial RO sources has addition-  
 99 ally grown to include satellites and constellations in near polar orbit (e.g., Angling et  
 100 al., 2021), promoting their use within DA experiments quantifying their benefit, i.e., RO  
 101 Modeling EXperiment (ROMEX) (Anthes et al., 2023).

102 RO soundings have provided a wealth of ionospheric information to produce 3-dimensional,  
 103 global observations of the ionosphere. During an RO sounding, the slant TEC is mea-  
 104 sured along the radio signal's limb sounding geometry connecting the GNSS satellite and  
 105 the observing LEO satellite. Electron density profiles (EDPs) are consequently retrieved  
 106 from these slant TEC observations at the ray tangent point locations through Abel in-  
 107 version, with this inversion relying on a spherical symmetry assumption. RO EDPs are  
 108 highly accurate observations of the ionosphere's F-region, generally around 300-400 km  
 109 altitude, especially for  $F_2$  region parameters  $N_mF_2$  and  $h_mF_2$  (Cherniak et al., 2021; Yue  
 110 et al., 2010; Lei et al., 2007). Relatively large errors can exist for low altitudes, i.e., the  
 111 E-region below 200 km altitude (Kelley et al., 2009). Large RO EDP errors are also re-  
 112 ported where there are breakdowns in the spherical symmetry assumption such as near  
 113 equatorial latitudes (Tsai et al., 2001; Tsai & Tsai, 2004) and beneath the crests of the  
 114 equatorial ionization anomaly (EIA), peaking at 200% (Liu et al., 2010; Yue et al., 2010).  
 115 Recent algorithm improvements have been made to the Abel inversion retrieval, aided  
 116 by prior ionosphere information (e.g., Yue et al., 2013; Pedatella et al., 2015; Chou et  
 117 al., 2017; Lin et al., 2020; Tulasi Ram et al., 2016), or using a bottom-up retrieval for  
 118 the D- and E-regions (Wu, 2018).

OSSEs have been used to quantitatively evaluate the value of RO observations (e.g., Yue, Schreiner, Kuo, et al., 2014; Lee et al., 2013; Hsu et al., 2018; He et al., 2019; Lin et al., 2015, 2017; Scherliess et al., 2004; Pedatella et al., 2020; Forsythe et al., 2021). Within an OSSE, synthetic data are generated from a nature run model simulation (that serves as a truth model) and then assimilated into a biased forecast model to assess improvement. Yue, Schreiner, Kuo, et al. (2014) performed an OSSE study prior to the launch of F7/C2, assessing the multiple planned RO EDPs from F7/C2 using NeQuick model as the nature run and assimilating EDPs into the empirical ionospheric model IRI. Lee et al. (2013) assimilated synthetic F7/C2 EDPs into a coupled ionosphere-thermosphere (I-T) physics-based model, and saw global improvements in electron density states over previous F3/C EDPs. Further to realistically assess the value of observing systems, it is crucial to quantify observation errors for DA. In particular, RO EDP assimilation can be negatively impacted by Abel retrieval errors if not properly characterized, with most recent RO error quantification performed in Yue et al. (2010); Liu et al. (2010). Even though OSSEs have been proven to be useful for mission planning and in informing the most effective constellations designs, previous OSSE work has yet to account for both forecast model errors and Abel retrieval errors in a comprehensive manner. For example, the tropospheric weather forecasting community has been investing considerable efforts to design standard and fair nature runs for OSSE studies (e.g., Masutani et al., 2007; Andersson & Masutani, 2010; Errico et al., 2013; Hoffman & Atlas, 2016). These standardized nature runs use state-of-the-art numerical model simulations that climatologically match the real atmosphere and contain realistic differences from the forecast model.

This study aims to evaluate the value of different RO constellation designs by quantifying the ionospheric specification impact of assimilating EDP observations into a coupled I-T model. We do this by adopting a comprehensive OSSE approach that overcomes the limitations of past RO EDP OSSE studies. The nature run is performed using the Whole Atmosphere Model-Ionosphere Plasmasphere Electrodynamics (WAM-IPE) (Akmaev, 2011; Maruyama et al., 2016), and the forecast coupled I-T model used in the DA framework is the Thermosphere Ionosphere Electrodynamics General Circulation Model (TIEGCM) developed by the National Center for Atmospheric Research (NCAR) (Qian et al., 2014; Richmond et al., 1992). Here, synthetic EDPs are retrieved from the WAM-IPE nature run simulation through an extensive Abel inversion procedure combined with simulated RO limb sounding geometries between the GNSS and hypothetical RO constellations. This Abel inversion procedure is built on the operational procedure used for the COSMIC-2 EDP data product. Synthetic EDP observations used in this study therefore include realistic Abel inversion errors, that cannot be represented by directly sampling electron density from the nature run at RO tangent points. We run a widely-used ensemble DA framework developed by NCAR’s Data Assimilation Research Testbed (DART) (Anderson et al., 2009) with TIEGCM, denoted as DART-TIEGCM. The Ensemble Adjustment Kalman Filter (EAKF) is used (Anderson, 2001). The OSSEs are run for a popularly studied event, the week of the March 2015 St. Patrick’s day storm. A total of ten OSSEs are performed for the different permutations of the four base virtual LEO constellation configurations. To address what constellation design is “best”, evaluated across different ionospheric regions, the results from these OSSEs are compared using various metrics including key ionospheric parameters of TEC,  $N_mF_2$  and  $h_mF_2$ , as well as the three-dimensional plasma density structure.

In the following sections, Section 2 provides details for the EDP Abel retrieval and its errors as well as the OSSE design. Section 3 provides the OSSE results, including assimilation impact, a relative OSSE ranking metric and a potential limit to observation impact. Section 4 contains general discussion assessing observation impact from DART-TIEGCM and Abel inversion errors, along with future work. Finally, Section 5 provides the conclusions.

## 171 2 Methods

### 172 2.1 Data Assimilation: DART-TIEGCM

173 In this study, we employ an ensemble-based approach, specifically the EAKF as  
 174 developed and implemented by DART (Anderson, 2001; Anderson et al., 2009). In  
 175 ensemble DA, states and their uncertainties are represented with ensembles in an Monte  
 176 Carlo approach tailored for high-dimensional state estimation. The typical cycle of the  
 177 EAKF consists of two steps: (1) the forecast step that propagates model states with the  
 178 full non-linear model dynamics and (2) the analysis step that optimally updates states  
 179 using observation information. The forecast step produces a forecast, or prior state, that  
 180 is used in the analysis step to produce an analysis estimate, or posterior. The DA cy-  
 181 cle continues, feeding the posterior into the next forecast step. In the EAKF, each ob-  
 182 servation has a spatially localised impact on model states determined by ensemble co-  
 183 variance information. This covariance information determines the statistical relationship  
 184 between an observation and nearby surrounding model states, and is dynamically esti-  
 185 mated from model ensembles that reflect nonlinear dynamics and physics.

186 We use the TIEGCM v2.0 developed by NCAR as the forecast model, solving a self-  
 187 consistent solution of first-principle equations of the I-T system and producing the three-  
 188 dimensional, time-varying field of the thermosphere and ionosphere states. The  $5^\circ$  res-  
 189 olution version of TIEGCM is used, with 29 pressure levels with half scale-height res-  
 190 olution that spans from  $\sim 97$  km to  $\sim 500$  km altitudes, depending on the solar con-  
 191 ditions. External forcing in TIEGCM is specified through solar ultraviolet irradiance pa-  
 192 rameterized with respect to a daily value of the F10.7 index (F10.7), and lower bound-  
 193 ary tides through the Global Scale Wave Model (GSWM). The magnetospheric forcing  
 194 is specified by the empirical Heelis convection model and an empirical auroral model.

### 195 2.2 Nature Run (Truth) Model: WAM-IPE

196 The nature run simulation, which serves as the truth model, is achieved with a free-  
 197 run of the I-T coupled physics-based model WAM-IPE developed by NOAA. There are  
 198 a number of differences in how the I-T physics and dynamics are solved between TIEGCM  
 199 and WAM-IPE. It is expected that these differences manifest as forecast model biases  
 200 and likely widen during the storm-period. WAM is a spectral whole atmosphere model,  
 201 containing 150 pressures levels that solves neutral states from the surface up to 400–  
 202 600 km altitudes, output at  $1^\circ$  horizontal resolution. IPE solves plasma state physics along  
 203 flux tubes in the semi-Lagrangian reference frame, extending up into the plasmasphere  
 204 encompassing 90 km to 10,000 km altitudes. In contrast, TIEGCM solves both neutral  
 205 and plasma states in the Euler reference frame, approximating the  $O^+$  flux at the up-  
 206 per boundary, and using lower boundary tide conditions specified by GSWM. In WAM-  
 207 IPE, solar irradiance is also parameterized using daily F10.7 but magnetospheric forc-  
 208 ing is specified by an empirical Weimer convection model driven by solar wind states at  
 209 1-minute cadence. These model differences are expected to introduce distinctive iono-  
 210 sphere biases partly corrected by assimilation of EDP observations.

### 211 2.3 Virtual Constellations

212 For this study, we use four base virtual LEO constellation configurations, derived  
 213 from the F3/C and F7/C2 constellations, to design ten different sets of hypothetical RO  
 214 constellation configurations. Each base constellation consists of six satellites with the  
 215 same inclination and altitude and at separate orbital planes. We simulate RO events be-  
 216 tween GPS and GLONASS and LEO satellite constellations in a similar mode of oper-  
 217 ation used by F7/C2. The base constellation parameters are as follows: (i) a 520 km al-  
 218 titude and  $24^\circ$  inclination constellation (similar to F7/C2), (ii) a 520 km altitude and  
 219  $72^\circ$  inclination constellation, (iii) a 800 km altitude and  $24^\circ$  inclination constellation, and

220 (iv) a 800 km altitude and 72° inclination constellation (similar to F3/C). All ten OSSE  
 221 combinations of one or two base virtual constellations are detailed in Table 1. Each OSSE  
 222 is referenced according to a short-hand notation, with the first two digits referencing the  
 223 constellation altitude, and the second two digits referencing the constellation inclination.  
 224 For instance, OSSE 1, with the short-hand notation 5024, is performed using the LEO  
 225 constellation of satellites at 520 km altitude and 24° inclination.

226 Within each OSSE, we assimilate EDPs from 160 km to 500 km altitude at 10 km  
 227 vertical sampling intervals to update the DART state vector containing electron density,  
 228  $e^-$ , and atomic oxygen ion,  $O^+$ . Gaussian uncorrelated noises are assigned to each elec-  
 229 tron density using the variances determined from the EDP uncertainty quantification  
 230 process detailed in Section 2.3.2. The RO tangent point locations for each of these base  
 231 constellations for a full day of observations is shown in Figure 1 to illustrate their respec-  
 232 tive coverage. As expected, the low-inclination constellations provide only low- and mid-  
 233 latitude observations, while the high-inclination constellations provide observations in  
 234 all latitude regions, at the cost of less dense spatial coverage.

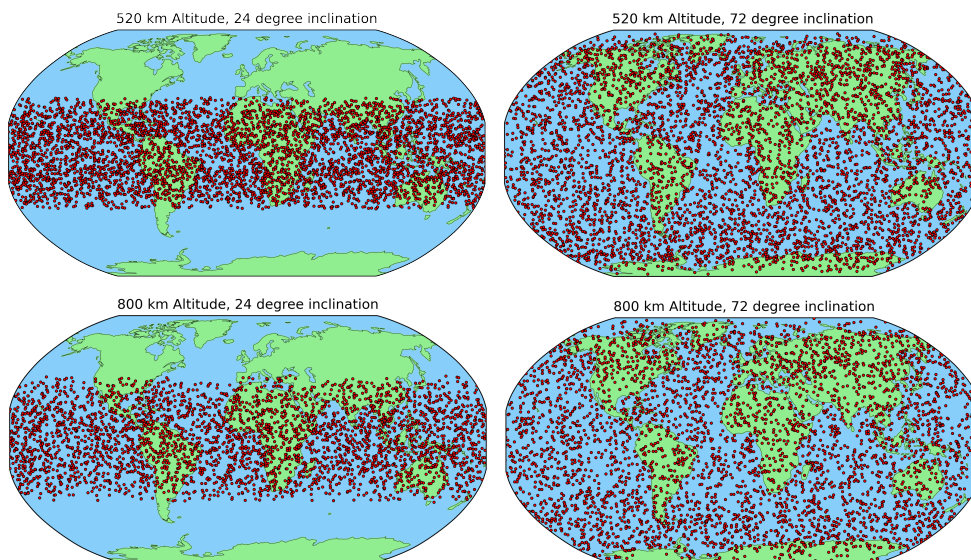


**Figure 1.** The RO observation tangent points shown for the full day of March 13th at 300 km altitude. Shown for the four base virtual LEO constellation configurations.

### 235 *2.3.1 Synthetic EDP Retrieval Using RO Simulation and Abel Inver-* 236 *sion*

237 Synthetic RO EDPs are generated from the WAM-IPE nature run simulation with  
 238 the typical EDP retrieval processes, as detailed in Hajj and Romans (1998); Schreiner  
 239 et al. (1999). Specifically, we use the Abel inversion algorithm adapted from the oper-  
 240 ational data product procedure used to generate ionPrf files from F3/C and F7/C2. The  
 241 sounding paths from GNSS satellites to LEO RO satellites are used to generate the syn-  
 242 thetic slant TEC profiles. For a typical RO sounding there is an occultation side and an  
 243 auxiliary side, where the auxiliary side passes through both the upper ionosphere and  
 244 plasmasphere and the occultation side passes through the ionosphere, atmosphere and  
 245 plasmasphere. Here, WAM-IPE's ionosphere extension provides plasmasphere informa-  
 246 tion. The resulting calibrated slant TEC profile comes from subtracting the auxiliary  
 247 side TEC profile from the occultation side TEC profile and contains only the impact of  
 248 the ionosphere. The synthetic EDPs are then retrieved by applying Abel inversion to these

**Table 1.** List of 10 OSSEs for different base LEO satellite constellation designs. For short-hand notation, the first two digits reference the constellation altitude and the last two digits reference the constellation inclination.

| Experiment Name | LEO Constellations                        | Short-Hand Notation |
|-----------------|---|---------------------|
| OSSE 1          | 520 km alt, 24° inc                       | 5024                |
| OSSE 2          | 520 km alt, 72° inc                       | 5072                |
| OSSE 3          | 800 km alt, 24° inc                       | 8024                |
| OSSE 4          | 800 km alt, 72° inc                       | 8072                |
| OSSE 5          | 520 km alt, 24° inc & 800 km alt, 72° inc | 5024 & 8072         |
| OSSE 6          | 520 km alt, 24° inc & 520 km alt, 72° inc | 5024 & 5072         |
| OSSE 7          | 520 km alt, 24° inc & 800 km alt, 24° inc | 5024 & 8024         |
| OSSE 8          | 800 km alt, 24° inc & 800 km alt, 72° inc | 8024 & 8072         |
| OSSE 9          | 520 km alt, 72° inc & 800 km alt, 72° inc | 5072 & 8072         |
| OSSE 10         | 520 km alt, 72° inc & 800 km alt, 24° inc | 5072 & 8024         |

249 synthetic calibrated slant TEC profiles. The synthetic EDP data retrieved in this study  
 250 thus contain the same systemic error as real ionPrf data products, ensuring the OSSE  
 251 results more closely reflect reality.

### 252 *2.3.2 Uncertainty Quantification of Synthetic EDPs*

253 To determine observation uncertainties necessary for DA, the EDP errors due to  
 254 Abel inversion are quantified. Observation errors are calculated using the difference be-  
 255 tween synthetic EDPs and the modeled electron density distribution from the WAM-IPE  
 256 nature run. Sample standard deviations are computed after binning difference data with  
 257 respect to the following parameters: day of year, constellation inclination, altitude, mag-  
 258 netic latitude, and solar local time. Four solar local time (LT) bins are used: LTs 4–  
 259 10, LTs 10–16, LTs 16–22, and LTs 22–4. LEO constellation altitude was found to  
 260 have a negligible effect on errors. Similar studies with EDP observations have used per-  
 261 centage errors over local time, altitude, and magnetic latitude (Lee et al., 2013; Liu et  
 262 al., 2010; Yue et al., 2010), while we quantify errors using standard deviation. Standard  
 263 deviations are computed from EDP samples within  $\pm 5$  km for a given altitude, and within  
 264  $\pm 5^\circ$  for a given latitude. An example of the calculated EDP uncertainties for March 13th  
 265 at 300 km is shown in Figure 2. Notable features is the distinct difference in the error  
 266 magnitude for the four solar local time bins and the impact that constellation inclina-  
 267 tion has on error magnitudes for the LT 16–22 in the equatorial latitudes. Over these  
 268 local times, there are highly variable spatial features such as the EIA and the prerever-  
 269 sal enhancement. The pronounced dependence on constellation inclinations can also be  
 270 due to smaller low-latitude observation counts for the high inclination orbit (shown in  
 271 Supporting Information (SI) Figure S1).

272 The Abel retrieval errors are furthermore characterized for  $N_m F_2$ ,  $h_m F_2$  and over  
 273 multiple EDP altitudes as shown in Figure 3. For  $N_m F_2$ , we see peak errors of 85% near  
 274 the south Atlantic anomaly (SAA), while the global error average is 18%, with structures  
 275 following Earth’s magnetic field lines. As expected, we see very small errors for  $h_m F_2$   
 276 with percentage errors peaking at 17% and averaging 4%. As for altitude variations of  
 277 errors, we see substantial errors at 200 km altitude, which is considerably higher than  
 278 past studies wherein they peak approximately at 200% (Liu et al., 2010; Yue et al., 2010).  
 279 Errors are smaller at 300 km, with peaks along the magnetic and near the SAA. Out-  
 280 side these two regions, errors are below 40%, with a median error of 25%. For 400 and  
 281 500 km altitudes, we see increasingly smaller errors, with a peak error near the SAA and

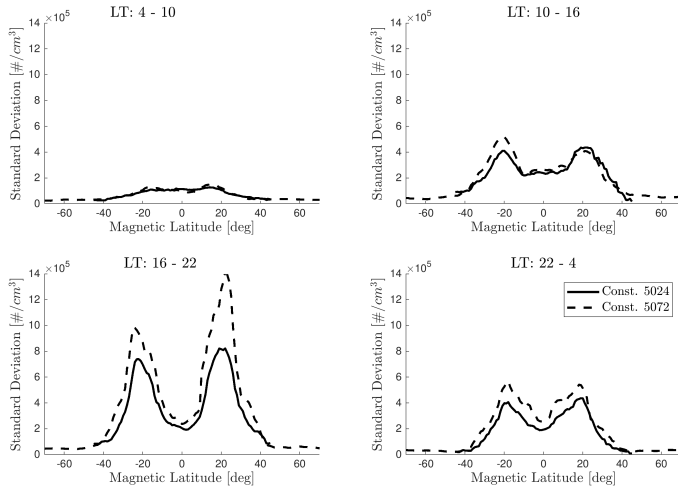


**Figure 2.** Standard deviations attributed to EDP observations. Shown for two constellations, 5024 and 5072, at 300 km altitude on March 13th. Standard deviations are computed from the difference between synthetic EDPs and plasma density from the WAM-IPE nature run simulation after binning data with respect to day of year, constellation inclination, altitude, magnetic latitude, and solar local time.

282 a global average of 17%. There are some spurious high errors seen at high latitudes where  
 283 there are low observation counts. It is noted these errors are highly dependent on solar  
 284 LT, with two example local time cases shown in SI Figures S2 and S3.

285 These large errors seen in Figure 3 come primarily from break-downs of the spherical  
 286 symmetry assumption used in Abel inversion. The break-downs of this assimilation  
 287 are expected to impact regions with large horizontal gradients in electron density dis-  
 288 tribution, such as near and below the magnetic equator and EIA. The impact is less acute  
 289 with increasing altitude. These errors are well-captured within uncertainty calculations  
 290 considered in this study. An additional source of RO errors are from on-board GNSS re-  
 291 ceivers as well as receiver errors, but these errors are not considered in this study.

## 292 2.4 Experiment Set-up

293 The OSSE period is the St. Patrick’s day storm of March 2015, with observed solar  
 294 and geomagnetic indices and solar wind states shown for this period in Figure 4. The  
 295 OSSE is broken into two periods, the preceding quiet period and storm-time. The quiet  
 296 period begins at UT00 on March 13th and ends at UT23 on March 16th. Localization  
 297 is done using the Gaspari-Cohn (GC) function (Gaspari & Cohn, 1999) with a GC ra-  
 298 dius of 0.2 radians ( $\sim 1300$  km) without vertical localization, so observations have im-  
 299 pact on all pressure levels. We do not use ensemble inflation. As the upper atmosphere  
 300 is strongly influenced by external forcing, we perturb solar irradiance with the F10.7 in-  
 301 dex and geomagnetic indices driven with the Heelis model for ensemble initialization with  
 302 90 members. These perturbations are normally distributed and kept constant through  
 303 the quiet period. The sampled F10.7 indices are sampled from  $d_{F10.7} \sim \mathcal{N}(120, 4^2)$  and  
 304 Heelis input is defined through the hemispheric power,  $d_{HP} \sim \mathcal{N}(22, 4^2)$  and the cross-  
 305 tail potential  $d_{\Phi} \sim \mathcal{N}(46, 8^2)$ . Ensembles are run through a 7-day spin-up period to reach  
 306 a steady-state for the start of the OSSE. For the storm period, magnetospheric drivers  
 307 have updated samples, sampling from  $d_{HP} \sim \mathcal{N}(115, 10^2)$  and  $d_{\Phi} \sim \mathcal{N}(135, 20^2)$  with  
 308 the same quiet period F10.7 samples.

309 Additional quality control is necessary for DA with observation flags and rejection  
 310 to avoid assimilating poor quality observations. We reject observations for three reasons:  
 311 negative values, outside an outlier threshold, and a failed forward operator, with rejec-  
 312 tion rates shown in Figure 5a. Negative values are the most common reason for rejec-  
 313 tion, notably at low altitudes where observation quality is worst. Between 10–50% of

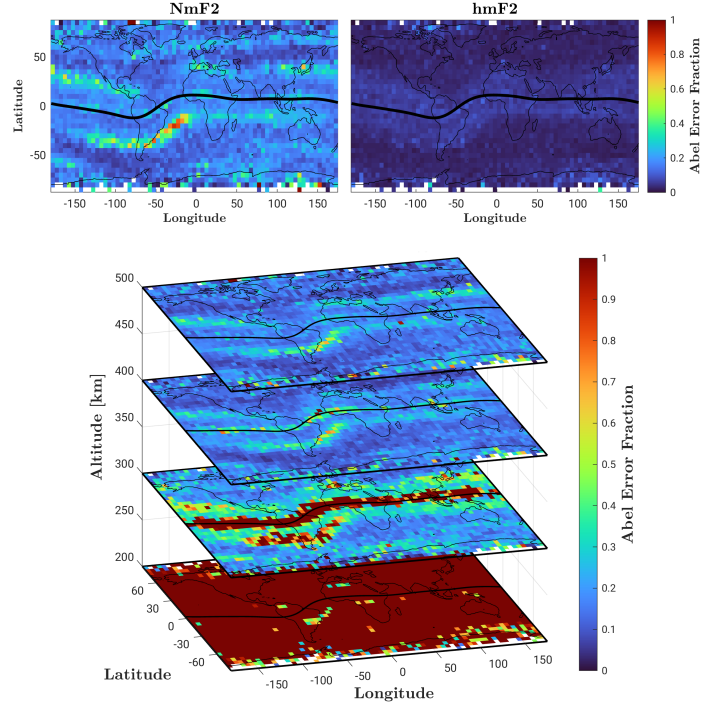


**Figure 3.** Binned average fractional error due to Abel retrieval, across all local times. Shown for  $N_mF_2$ ,  $h_mF_2$  and at each EDP altitude. Black line indicates the magnetic equator. Blank regions are due to lack of observation coverage.

314 observations are rejected between 160 – 250 km altitude, with rejection rates consid-  
 315 erably improving at higher altitudes. We reject very far off observations using a 10 stan-  
 316 dard deviation threshold. For OSSE observation counts shown in Figure 5b, 520 km alti-  
 317 tude constellations show greater observation counts than the 800 km altitude constel-  
 318 lations.

### 319 3 OSSE Results

#### 320 3.1 OSSE Ionospheric Results

321 First highlighting the quiet period, we show the impact of the first analysis step  
 322 at UT01 on March 13th in Figure 6, for 300 km altitude. In the top row is the WAM-  
 323 IPE nature run, where synthetic observations are derived, and the no-assimilation con-  
 324 trol (identical to the prior here), for electron densities at 300 km altitude. In the mid-  
 325 dle row are the posterior electron densities for OSSEs 1-4, each containing a single con-  
 326 stellations. A first notable bias between WAM-IPE and TIEGCM control is the EIA, where  
 327 WAM-IPE produces higher magnitudes and sharper horizontal gradients. High electron  
 328 densities additionally extend into the night-side for WAM-IPE. In contrast, TIEGCM  
 329 has a less prominent EIA peak and smoother spatial gradients, stretching for longer length  
 330 scales, and has EIA peaks westward of WAM-IPE's. Comparing electron density mag-  
 331 nitudes between TIEGCM and WAM-IPE, TIEGCM under-represents electron densities on the day-side  
 332 and over-represents electron densities on the night-side. Assessing the posterior electron density  
 333 states, seen in the middle row of Figure 6, the analysis step  
 334 is as expected positively impacting posterior states, such as in increasing the EIA mag-  
 335 nitude and better replicating the extension of higher electron density magnitudes into

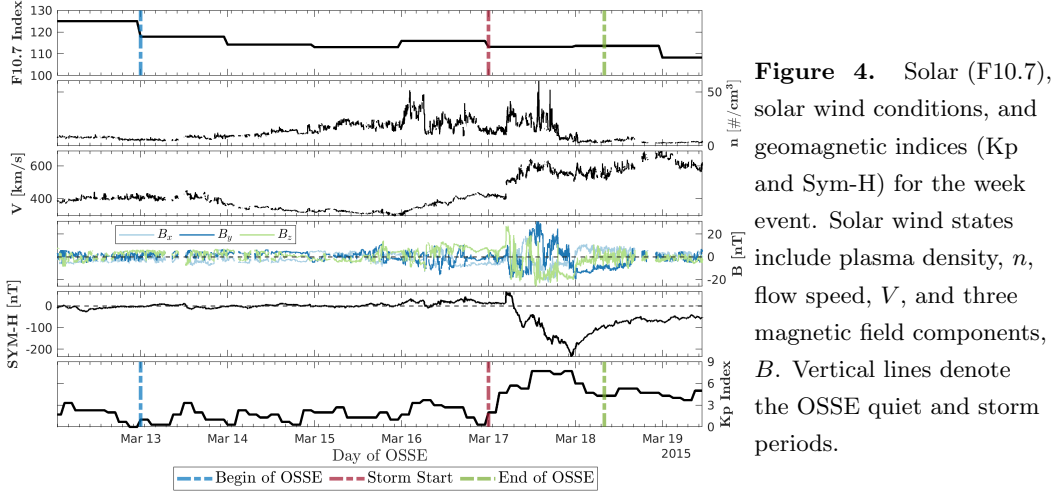


**Figure 4.** Solar (F10.7), solar wind conditions, and geomagnetic indices (Kp and Sym-H) for the week event. Solar wind states include plasma density,  $n$ , flow speed,  $V$ , and three magnetic field components,  $B$ . Vertical lines denote the OSSE quiet and storm periods.

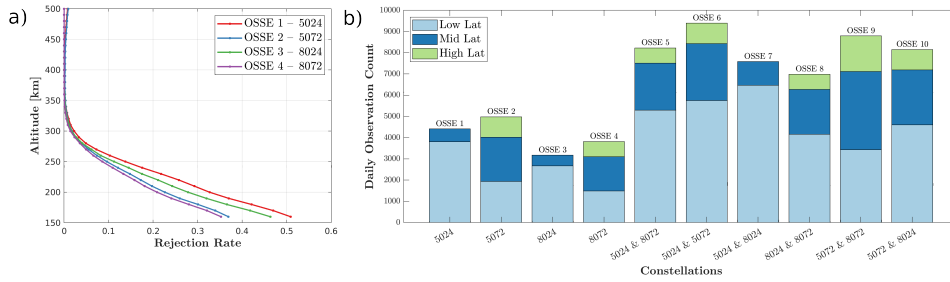


**Figure 5.** a) Shows the observation rejection rate as a function of altitude. b) Shows the daily EDP observation count for each OSSE constellation configuration, separated by latitude region.

336 the low-latitude night side. For high inclination constellations 5072 and 8072, electron  
 337 density magnitudes are noticeably reduced in the night side high-latitudes.

338 Illustrating the performance of the analysis update is shown in the bottom row of  
 339 Figure 6. The analysis bias improvement is defined as

$$340 \quad \text{Bias Improve} = |\bar{\mathbf{x}}^{prior} - \mathbf{x}^{NR}| - |\bar{\mathbf{x}}^{post} - \mathbf{x}^{NR}| \quad (1)$$

341 where  $|\mathbf{x}|$  is the element-wise absolute value of mean OSSE state vectors  $\bar{\mathbf{x}}^{prior}$ ,  $\bar{\mathbf{x}}^{post} \in$   
 342  $\mathbb{R}^n$  and nature run state vector  $\mathbf{x}^{NR} \in \mathbb{R}^n$ . Bias improvement is shown in the bottom  
 343 row of Figure 6, where blue regions indicate improved electron density biases and red  
 344 regions indicated worsened biases. For state grid point comparisons between the two mod-  
 345 els, we down-sample WAM-IPE and interpolate as needed to TIEGCM's  $5^\circ$  grid reso-  
 346 lution. At locations where WAM-IPE shows large electron density magnitudes, biases  
 347 overall improve when observations are available. This is most evident for constellations  
 348 5024 and 8024 at peak EIA magnitudes. In red regions directly off WAM-IPE's EIA, we  
 349 see the analysis step worsen biases. Generally, there are red worsen regions where there  
 350 is a large gradient in WAM-IPE electron densities. More discussion of these worsening  
 351 regions is addressed in Section 4, and is largely explained by Abel retrieval errors and  
 352 improper background covariance. A similar figure for the storm period is shown in SI  
 353 Figure S4.

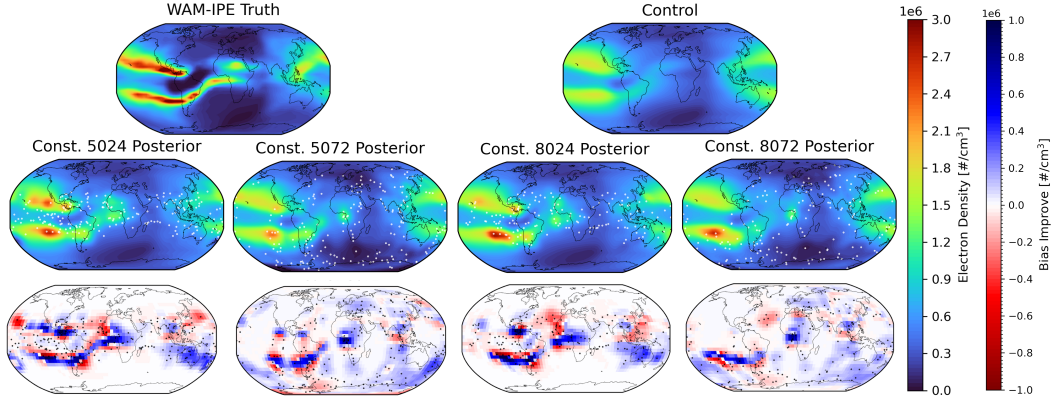


**Figure 6.** Electron density shown for the nature run, control, and OSSEs 1-4 posteriors at 300 km altitude at UT01 on March 13th, the first analysis step. The middle row shows posterior states, where white points are the assimilated tangent-point observations at 300 km altitude. Bias improvement, shown on bottom row, is illustrated with blue regions providing improvement and red regions worsening.

As the primary metric to assess OSSE performance, we use the root mean-square error (RMSE) defined as

$$\text{RMSE} = \sqrt{\frac{\sum_{j=1}^N (x_j^{NR} - \bar{x}_j^{exp})^2}{N}} \quad (2)$$

where  $x_j^{NR}$  is the  $j$ th WAM-IPE state,  $\bar{x}_j^{exp}$  is the  $j$ th ensemble mean OSSE state, and  $N$  is the total number of states. As RMSE is a magnitude dependent quantity, we separate results into three latitudes regions, where low latitude is between  $-30^\circ$  and  $+30^\circ$ , middle latitude is between  $-30^\circ$  and  $-60^\circ$  as well as  $30^\circ$  and  $+60^\circ$ , and high latitude is below  $-60^\circ$  and above  $60^\circ$ . We show results for  $N_mF_2$ ,  $h_mF_2$ , TEC, and altitude electron densities. We compare relative posterior RMSE performance against a no-assimilation control.

The  $N_mF_2$  RMSE for all ten OSSEs is shown in Figure 7 for both quiet and storm periods. At high latitudes, the best performance is seen from OSSE 9 including constellations 5072 & 8072, the constellations with the most high-latitude coverage. As expected, OSSEs 1, 3 and 7 have no high-latitude coverage resulting in negligible impact on high-latitude errors. At low latitudes, OSSE 7, containing constellations 5024 & 8024, performs the best with the highest coverage of observations. Additionally, OSSEs 3 and 4 containing only constellations 5072 & 8072 have the least improvement in errors. At mid-latitudes, the OSSEs containing just constellations 5024 or 8024 have the worst performance, OSSEs 1,3 and 7. High inclination OSSEs show consistent improvement in  $N_mF_2$  RMSE at low-latitudes and in high-latitudes.

The  $N_mF_2$  posterior RMSEs for the storm period are also shown in Figure 7. As with the quiet period at low- and high-latitudes, there is a consistent improvement in RMSE over the control for the storm period, with more observation coverage of a region providing better performance. OSSE 7 with constellations 5024 & 8024 performs the best at low latitudes, and OSSE 9 with constellations 5072 & 8072 performs the best at high latitudes. It is also noted that the control RMSE increases for the storm-period due to increasing model biases between TIEGCM and WAM-IPE.

Further RMSE time-series plots are available in the SI Figures S5-S10. The TEC RMSE time series is shown in SI Figure S5, showing very similar performance to  $N_mF_2$

383 RMSEs.  $h_m F_2$  RMSEs are additionally shown in Supporting Plots S6. For  $h_m F_2$ , we see  
 384 only slight impact to posterior RMSEs as compared with the no-assimilation control. This  
 385 negligible performance is primarily attributed to a lack of state spread in  $h_m F_2$ , as we  
 386 expect  $h_m F_2$  observation quality to be very high, see Figure 3. Additional figures, in-  
 387 cluding RMSE at each altitude (200, 300, 400 and 500 km) are available in the SI Fig-  
 388 ures S7, S8, S9 and S10. Altitude RMSEs show similar performance results as the  $N_m F_2$   
 389 RMSEs with the exception of 200 km altitude.

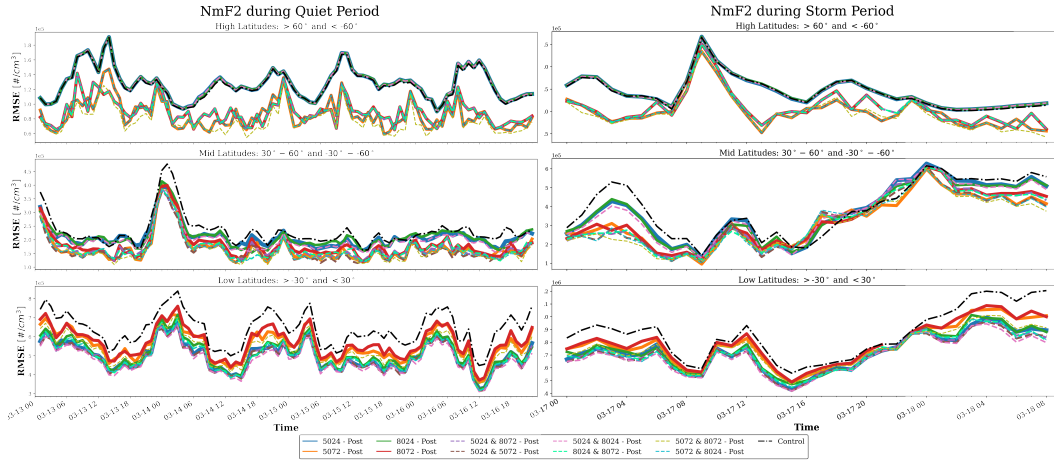


**Figure 7.** The  $N_m F_2$  RMSE for each OSSE throughout the quiet period (left) and storm period (right). Solid lines indicate single constellation OSSEs and dashed lines indicate two constellation OSSEs. Performance is assessed compared to a no-assimilation control in the dashed black curve.

390 Observation comparisons at 200 km and 400 km altitude are shown in Figure 8,  
 391 created through collecting all quiet-period observations at a given altitude. Here, IPE  
 392 electron density states at EDP observation tangent points are shown against the Abel  
 393 retrieval, TIEGCM prior and TIEGCM posterior, and separated by latitude region. Each  
 394 plot is a density map of the observations in each range, normalized by the respective max  
 395 binned observation count, shown in units of  $10^5 \text{ cm}^{-3}$ . The goodness of fit to the line  
 396  $x = y$ ,  $R^2$ , and the number of observations,  $N$ , are provided for each sub-figure. For  
 397 400 km altitude, there is quite good agreement among the IPE states and Abel retrievals.  
 398 TIEGCM prior biases are most noticeable at the low latitudes and for the 400 km alti-  
 399 tudes there is consistent improvement in posterior agreement and  $R^2$ . Posterior states  
 400 at 400 km perform best at the high latitudes and worst at low latitudes, likely due to  
 401 EIA biases. We see all Abel retrieval values of  $R^2$  greater than or equal to 0.78. Obser-  
 402 vation comparisons for 300 and 500 km altitudes are shown in SI Figure S11 and show  
 403 similar results to 400 km altitude.

404 In the left sub-figure of Figure 8 for 200 km altitude, we see very different results.  
 405 For all latitude regions, the Abel retrieval and TIEGCM prior and posterior are all severely  
 406 underbiased to IPE nature run electron densities. Still, we do see improvement in agree-  
 407 ment for posterior states at the middle and high latitudes, while the 200 km low latitudes  
 408 show worsening error. The low and middle latitudes priors have surprising good  $R^2$  val-  
 409 ues, due to many states being very low magnitude (not very visible on this plot axis scale),  
 410 while the Abel retrieval at low latitudes has a negative  $R^2$  value.

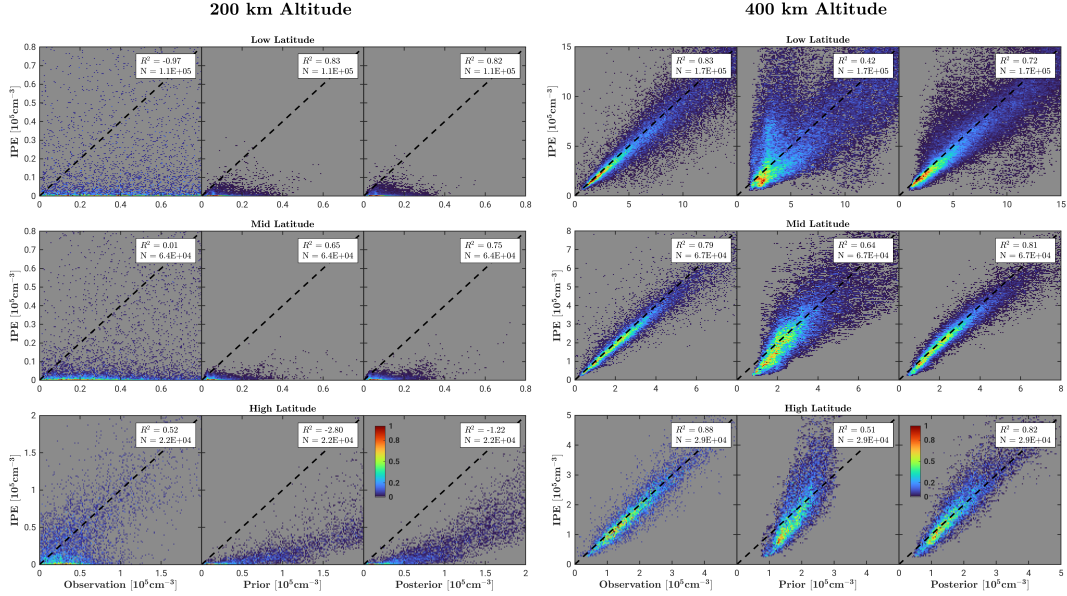


**Figure 8.** Comparison of electron density observations at given altitudes (200 and 400 km), with the nature run IPE state shown against the Abel retrieval, TIEGCM prior and TIEGCM posterior states. Density heat maps are shown, with counts normalized by the max bin count for that subplot. Units are all in  $10^5 \text{cm}^{-3}$ .

411

### 3.2 Ranking Metric

412

413

414

415

416

417

418

To further quantify relative OSSE performance, we devise a simple high-level ranking metric. Using the time series of RMSEs calculated for  $N_m F_2$ ,  $h_m F_2$ , TEC and altitude electron densities, each OSSE is ranked for each hour. The ten OSSEs are ordered and ranked according to each OSSE’s RMSE, 1 through 10, with 1 having the lowest error (best performance) and 10 having the highest error (worst performance). Averaging hourly OSSE ranks over the whole experiment period then gives the ranking metric.

419

420

421

422

423

424

425

426

427

428

429

430

431

432

The vertically integrated TEC ranking metric is shown in Figure 9 for the three latitude bins and globally, for both the quiet and storm periods. Table cells are color-coded with deep green indicating the best performance (close to 1) and deep red indicating worst performance (close to 10). For low latitudes, OSSE 7 (5024 & 8024) performs the best with the highest coverage of low latitudes. For high latitudes, OSSE 9 (5072 & 8072) performs the best with the highest coverage in that respective region. OSSEs that mix high and low inclination constellations, OSSE 5, 6, 8 and 10, generally do well across the board. OSSE performances are similar for quiet and storm conditions as most quiet and storm rankings are within a rank of 1. For global rankings, these typically reflect performance at the low and mid-latitudes, where the largest electron density magnitudes are present and thus dominate RMSEs. Additional ranking metric tables are available for  $N_m F_2$ ,  $h_m F_2$  and electron density at altitudes 200, 300, 400 and 500 km in SI Figures S12, S13 and S14. It is noted that TEC,  $N_m F_2$  and 300-500 km altitude ranking values all indicated similar results.

433

434

435

436

To explain ranking metrics performance, we collect all the rankings for the quiet period at 200, 300, 400 and 500 km electron density altitudes (SI Figure S12) and plot them against their daily average observation count, shown in Figure 10. The left sub-figure shows results collected for altitudes 300, 400 and 500 km, and the right shows rank-

| Experiment Name | Constellations | Low Lat | Mid Lat | High Lat | Global | Low Lat | Mid Lat | High Lat | Global |
|-----------------|----------------|---------|---------|----------|--------|---------|---------|----------|--------|
|                 |                | Quiet   |         |          |        | Storm   |         |          |        |
| OSSE 1          | 5024           | 4.98    | 9.31    | 8.8      | 5.85   | 5.7     | 8.42    | 8.58     | 6.79   |
| OSSE 2          | 5072           | 9.09    | 5.37    | 3.97     | 9.03   | 7.97    | 4.09    | 3.06     | 7.09   |
| OSSE 3          | 8024           | 6.8     | 9.28    | 8.96     | 7.24   | 5.82    | 6.94    | 9.06     | 6.48   |
| OSSE 4          | 8072           | 9.91    | 6.9     | 4.27     | 9.91   | 9.67    | 5.18    | 4.55     | 9.03   |
| OSSE 5          | 5024 & 8072    | 3.6     | 4       | 4.84     | 3.05   | 4.91    | 6.3     | 5.42     | 4.88   |
| OSSE 6          | 5024 & 5072    | 2.27    | 2.55    | 4.37     | 1.64   | 3.09    | 4.7     | 3.85     | 2.76   |
| OSSE 7          | 5024 & 8024    | 1.34    | 7.71    | 8.93     | 2.79   | 2.21    | 7.82    | 8.73     | 4.42   |
| OSSE 8          | 8024 & 8072    | 5.43    | 4.53    | 4.55     | 4.93   | 4.85    | 5.15    | 5.48     | 4.82   |
| OSSE 9          | 5072 & 8072    | 7.83    | 2.31    | 2.19     | 7.43   | 7.33    | 2.82    | 2.45     | 5.94   |
| OSSE 10         | 5072 & 8024    | 3.77    | 2.81    | 4.13     | 3.13   | 3.45    | 3.58    | 3.82     | 2.79   |

**Figure 9.** OSSE ranking metric for TEC. Rankings are averaged over the quiet period defined from March 13th UT01 to March 16th UT022 and averaged over the storm period defined from March 17th UT00 to March 18th UT08. Values close to 1 indicate the best performance and values close to 10 indicate the worst performance.

ings for 200 km, also splitting for low, mid and high latitudes. Very simply, where we have more observation, we see better OSSE performance with lower metric ranks as shown with a strong negative correlation. This finding holds for all regions except for one: 200 km altitude at low latitudes. These values are reflected in SI Figure S12 where worsening ranking is seen for 200 km in OSSEs, as well as in Figure 8 at 200 km with little agreement between IPE states and Abel retrieved EDPs. Regardless, we still do see improvement in the ranking metric at 200 km altitudes for mid- and high-latitudes, same as all other regions improving performance with greater observation coverage.

A couple of additional results are as follows. First, we see more observations from the 520 km altitude constellations than the 800 km altitude constellations, and this directly corresponds to better ranking metrics for these OSSEs. With this, it is arguable that OSSE 6 with 5024 & 5072 is the best performing OSSE (as reflected in the global ranking metric in Figure 9). We see constellation 8024 have 27% less profiles than constellation 5024; we see constellation 8072 have 24% less profiles than constellation 5072. The differences is likely explained by the shorter orbit period of the 520 km altitude constellations, enabling more limb passes and RO events. Secondly, OSSE 9 with 5072 & 8072 performs poorly for low latitude observations, as one might expect; however from Figure 5, OSSE 9 performs worse than OSSEs 1 (5024) and 3 (8024) with comparable low-latitude coverage. This worse performance can potentially be explained by larger observation errors that the high inclination constellations show at low-latitudes, as illustrated most evidently in the bottom left panel of Figure 2. Thus a combination of a low- and high-inclination constellation provides the best global coverage.

### 3.3 Observation Performance Limit

An additional question raised when designing an observing system and adding more observations: what is the potential performance limit? We define a “performance limit” as the point when assimilating more observations plateaus improving OSSE errors. To address this question with available OSSE results, we compute the RMSE for all grid points for the low-, mid- and high-latitude regions of each OSSE, as well as for the con-

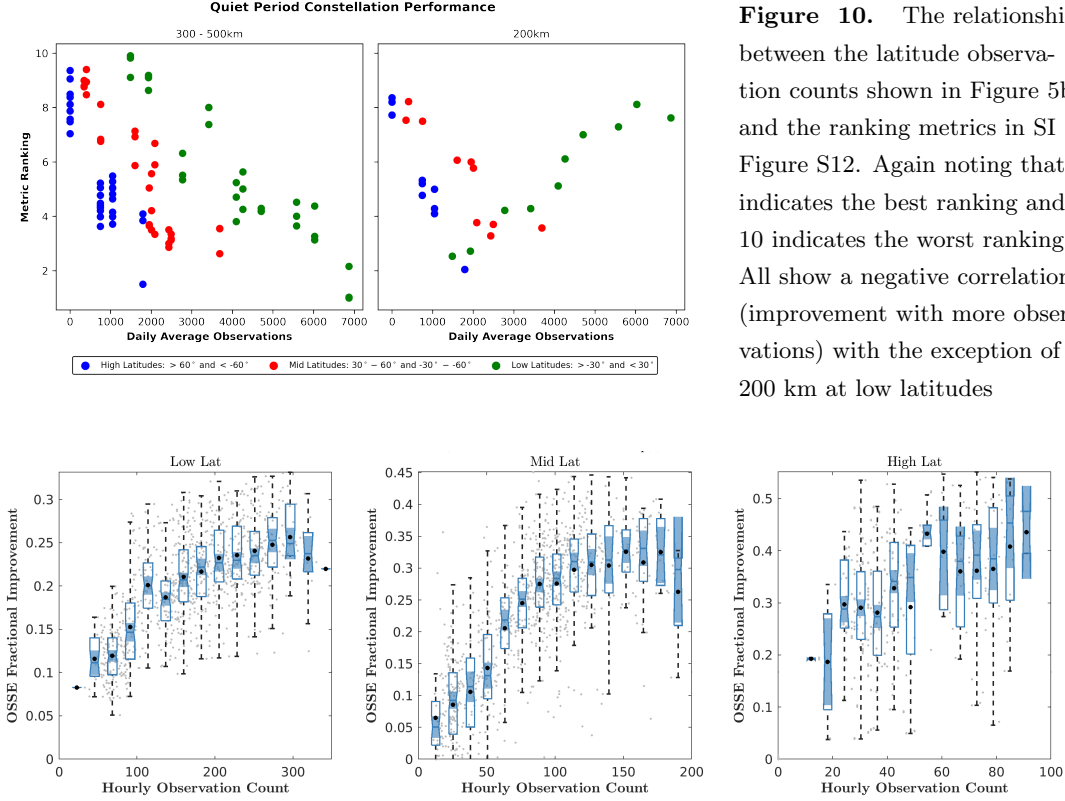


**Figure 10.** The relationship between the latitude observation counts shown in Figure 5b and the ranking metrics in SI Figure S12. Again noting that 1 indicates the best ranking and 10 indicates the worst ranking. All show a negative correlation (improvement with more observations) with the exception of 200 km at low latitudes

**Figure 11.** OSSE  $N_mF_2$  RMSE fractional improvement over the control as a function of observation count, defined in Equation 3. Calculated for the entire  $N_mF_2$  grid RMSE within each latitude band. Mean improvement (black dots) and notched box plots are averaged over count bins of all samples (grey dots). Non-overlapping shaded regions indicate the significant difference between medians (5% confidence).

465 trol. We then define the OSSE fractional improvement over the control as

466 
$$\text{Fractional Improvement} = \frac{\text{RMSE}_{ctrl} - \text{RMSE}_{exp}}{\text{RMSE}_{ctrl}} \quad (3)$$

467 This is done for every hour of the OSSE and all ten OSSEs. Next binning over hourly  
 468 observation counts we show the mean and notched box plot for the  $N_mF_2$  RMSEs in Fig-  
 469 ure 11. For the low- and mid-latitudes, there is a steady improvement in performance  
 470 with more observations and a visible leveling off, as the improvement is no longer sta-  
 471 tistically significant at the peak observation counts. It is noted for the end points of each  
 472 latitude region, shaded regions have very small or very large spread due to a limited num-  
 473 ber of samples. For high latitudes, the results are more noisy as we have less samples due  
 474 having only two constellations with high-latitude coverage. We see a positive trend in  
 475 the high-latitude fractional improvement that does not appear to plateau. Results for  
 476 TEC show very similar results to  $N_mF_2$  (SI Figure S15), and  $h_mF_2$  fractional improve-  
 477 ment are less consistent (SI Figure S16). Further study is needed to investigate the cause  
 478 of this performance limit, such as due to observation errors, background covariance, lo-  
 479 calization and other DA parameters, model errors, model resolution, or observation spa-  
 480 tial density.

## 481 4 Discussion

482 Returning to the initial question we first posed as to what constellation configu-  
 483 ration is best: it depends. Simply put, with more observation coverage in a given region,  
 484 we gain better ionosphere specification, with a combination of a low- and high-inclination  
 485 constellation providing the best global coverage. Therefore, designing an RO constella-  
 486 tion observing system depends on what regions we desire to study or monitor.

487 Fully simulating the Abel inversion retrieval for EDP observations allows us to eval-  
 488 uate the impact of Abel inversion errors within a DA framework, as compared with stud-  
 489 ies such as Hsu et al. (2014); Lee et al. (2013) that only perturbed using Gaussian er-  
 490 rors. Previously documented Abel inversion errors are evident, notably at the low lat-  
 491 itudes and low altitudes (Tsai et al., 2001), and their resulting in poor analysis updates.  
 492 Abel inversion particularly has trouble reproducing the low electron densities in “plasma  
 493 caves” beneath the EIA crests (Liu et al., 2010; Yue et al., 2010), as this is the one the  
 494 one region (200 km, low latitude) we see the DA have negative impact on electron den-  
 495 sity states. These were also expected from Figure 3 where there are considerably high  
 496 Abel retrieval errors. Nevertheless, we do see positive impact for 200 km altitudes at the  
 497 mid and high latitudes. Additionally as we move to higher altitudes, we see observations  
 498 consistently provide positive data impact.

499 OSSE results suggest this region of very low electron densities is likely an inher-  
 500 ent limitation of RO and the Abel inversion technique. As we move to lower altitudes,  
 501 the radio signal passes becoming increasing longer, comprising more of the ionosphere  
 502 and yielding larger slant TEC observations. The Abel retrieved EDPs cannot the resolve  
 503 IPE’s low electron densities using large TEC observations, especially if the spherical sym-  
 504 metry assumption is increasingly broken, adding increasingly more observation noise. We  
 505 also see many negative observations in this region, reducing data available for assimi-  
 506 lation. Therefore we see RO EDPs to not be useful for ionospheric specification in this  
 507 low latitude, low altitude region, supporting the conclusions of Lee et al. (2012).

508 To detail poor EDP performance, we highlight two assimilated profiles shown in  
 509 Figure 12. We focus on the worsening regions of constellation 5024 from Figure 6. We  
 510 show the WAM-IPE nature run, Abel retrieval, and the TIEGCM prior and posterior  
 511 at profile locations.

512 One source of poor analysis updates come from DART-TIEGCM, exhibited by pro-  
 513 file (a) of Figure 12. At this location, there is good agreement between the Abel retrieved  
 514 EDP (and its assigned 1 standard deviation (std) uncertainty) and the IPE nature run.  
 515 This observation point is within EIA peak electron density, and as the EAKF locally up-  
 516 dates states using the ensemble background covariance, an over-correction is performed  
 517 for grid points off IPE’s EIA structure. The regional impact of this observation is shown  
 518 in the bottom plot of Figure 12, including the nature run IPE state at 300 km, TIEGCM’s  
 519 background electron density correlation and the observation increment. TIEGCM shows  
 520 high background correlations extending beyond IPE’s sharper electron density gradient,  
 521 and the update is very much defined by the isotropic GC localization. This poor update  
 522 underscore the importance of having a good background covariance, and is a necessary  
 523 filter feature for global specification. Many studies have been devoted to improving the  
 524 local update impact, either through improved background covariance or through local-  
 525 ization (e.g., Lin et al., 2015; Hsu et al., 2018; Forsythe et al., 2020; Zhang et al., 2023).

526 Another source of poor analysis updates, one very much a focus of this study, come  
 527 from Abel inversion errors, shown at point (b) of Figure 12. At this location, the prior  
 528 EDP has fine agreement with IPE; however, the Abel inverted EDP is considerably more  
 529 biased, and we see worse posterior error. This profile deviates from the typical Chap-  
 530 man function, instead showing a double peak structure in both the EDP observation and  
 531 IPE RO tangent points. A view of this profile and the IPE states are shown in SI Fig-

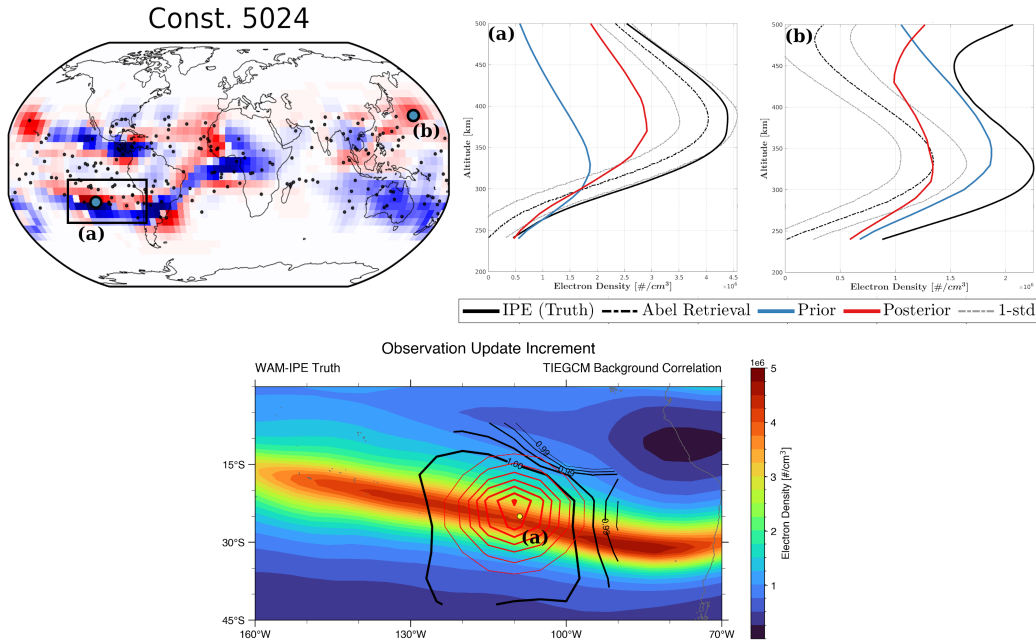


**Figure 12.** Highlighting two EDPs introducing poor analysis updates. Shown using first analysis step of constellation 5024 (same as in Figure 6). EDP (a) highlights poor background covariance, EDP (b) highlights large Abel inversion error. Bottom contour plot shows the IPE electron density at 300 km, and the observation increment (red) and TIEGCM background correlation (black).

532 ure S17, where the tangent points’ quasi-vertical profile at high altitudes includes higher  
 533 magnitude electron densities. Ideally, this observation profile should be flagged for qual-  
 534 ity control and not assimilated, or alternatively the observation uncertainty should be  
 535 considerably increased to more sufficiently account for the Abel inversion error.

536 It is noted as a caveat that the devised ranking metrics only provides a big-picture  
 537 view of the relative OSSE results. These rankings do not indicate the magnitude of the  
 538 relative OSSE performance, and should be viewed in conjunction with the RMSE time  
 539 series plots to gain a full perspective. Regardless, conclusions from these rankings gen-  
 540 erally support the findings from the RMSE time-series. Additionally assessing errors through  
 541 RMSE and with parameters TEC and  $N_m F_2$  can simplify the global impression of iono-  
 542 sphere specification. These metrics are decidedly magnitude dependent, sometimes rep-  
 543 resenting only the highest magnitude locations, e.g., the EIA or  $F_2$  peak. The altitude  
 544 profile of the electron density can be very important for space weather influences, mak-  
 545 ing ionospheric specification a three-dimensional problem needing to be address through  
 546 multiple metrics.

547 We focus in this study on the relative performance of all OSSEs, and the filter per-  
 548 formed well enough for assessment. Filter features such as tuned localization, implemen-  
 549 ting inflation, and better ensemble initialization with more realistic geomagnetic forcing  
 550 would all help to improve data impact of the synthetic EDPs. One evident source of poor  
 551 impact is with the lack of  $h_m F_2$  spread in TIEGCM, as previously noted in Lee et al.  
 552 (2012), that causes  $h_m F_2$  improvement to be considerably less than expected given their  
 553 low errors.

Another large restriction in filter performance was achieving sustained RMSE improvement from using a coupled I-T model due to plasma states have limited memory in the system. Non-updated neutral states in TIEGCM quickly rebound posterior plasma states back to control states in the forecast step, showing only a 1-2 hour system memory. Previous studies have shown plasma forecasting only on the order of hours with ionosphere assimilation in coupled I-T models (Jee et al., 2007; Chartier et al., 2013). Neutral states have a longer forecasting memory (Chartier et al., 2013), and specifying neutral states such as oxygen composition have been shown to greatly improve plasma forecasting (Hsu et al., 2014). This would help the system to retain plasma RMSE improvements when forecasting and see greater OSSE performance. Another possibility not included in this study is the potential to estimate neutral states using the EDP observations, and has been shown to have positive impact for composition, neutral temperature, and neutral winds (Matsuo & Hsu, 2021; Dietrich et al., 2022).

Accounting for realistic Abel inversion and forecast model errors in this study underscores the need for more complete EDP error quantification and observation quality control. There still remains work needed to fully quantify Abel inversion errors, and quantify their impacts from breakdowns in the spherical symmetry assumption. In this study there are two main error sources included in these OSSEs: errors from Abel inversion and errors within the DART-TIEGCM DA framework, and it is challenging to fully deconvolve these two error sources. Future OSSE work could apply the same OSSE setup while also running equivalent OSSEs with synthetic EDPs directly sampled at WAM-IPE locations, enabling direct comparisons of error impacts and more complete quantification of Abel inversion errors. Abel error fitting over altitude, magnetic latitude and local time, as in Yue et al. (2010); Liu et al. (2010), was shown to not be sufficient in some cases. Additional error analysis capturing exactly how the spherical symmetry assumption is being broken is needed by analyzing the radio ray paths taken through the ionosphere. Better quantification of these Abel errors should improve DA performance in negatively impacted regions, and provide means for better observation quality control. Further, more advanced Abel inversion algorithms have improved low altitude observations errors and improved their DA impact (e.g., Pedatella et al., 2015; Wu, 2018; Chou et al., 2017; Tulasi Ram et al., 2016) and were not included in this study.

## 5 Conclusions

To inform future RO constellation mission planning and design, this study uses a comprehensive OSSE approach to evaluate the ionospheric specification impact of assimilating RO EDPs into a coupled I-T model. We perform ten OSSE configurations to evaluate four base hypothetical RO constellations. These RO constellations are modeled after F3/C and F7/C2, at either 24° or 72° inclination and at either 520 or 800 km altitude orbits. Each OSSE's relative performance is evaluated through multiple metrics during the St. Patrick's Day storm on March 13-18, 2015, including quiet and storm-time conditions, by using the DART-TIEGCM and a nature run simulation provided by WAM-IPE. This study is the first ionospheric OSSE study to comprehensively and realistically account for forecast model and observation errors by using a distinct nature run simulation and forecast model, as well as retrieving synthetic EDP observations from the WAM-IPE nature run with an extensive Abel inversion procedure.

Overall, better spatial coverage of EDP observations from a given RO constellation design corresponds to a better OSSE performance. For low-inclination constellations with greater low-latitude coverage, the best performance is obtained for the low latitude ionosphere, and likewise for high-inclination constellations the best performance is achieved for the high latitude ionosphere. The increased spatial coverage of EDPs directly corresponding to improved results is best reflected in a ranking metric, with higher observation counts seen for the 520 km altitude constellations, arguably making OSSE 6 (5024 & 5072) the best performing OSSE. This combination of a low- and high-inclination con-

606 stellation additionally provides the best global coverage. Consistent posterior improve-  
607 ment is seen at all latitudes for altitudes 300 to 500 km, demonstrating evident bene-  
608 fits to EDP assimilation. A performance limit is also conceivably illustrated for two 6-  
609 satellite constellations, and further study is needed to uncover its causes and validity.

610 Another notable finding is the limitations of RO EDP data impact on the dayside  
611 equatorial region at low altitudes. DA impact in this region is negatively impacted by  
612 worsening Abel inversion errors due to both breakdowns in the spherical symmetry as  
613 well as RO's inherent shortcoming in accurately retrieving very low, low altitude plasma  
614 densities. Additional large retrieval errors are seen when vertical plasma density struc-  
615 tures deviate from the typical Chapman function, such as double peaked EDPs.

616 Ultimately, RO EDPs offer a unique, three-dimensional global ionospheric perspec-  
617 tive advantageous for global ionospheric specification. While Abel retrieval and uncer-  
618 tainty quantification may still be improved, as considered in the discussion, RO EDPs  
619 offer clear operational space weather benefits for the upper atmosphere. Further assess-  
620 ment of space weather observing systems using comprehensive OSSE studies will con-  
621 siderably enhance future observation integration into DA systems, as well as greatly aid  
622 in future constellation design.

## Open Research Section

Software tools used for the work are all publicly available. The Whole Atmosphere Model Ionosphere Plasmasphere Electrodynamics (WAM-IPE) software was developed by the NOAA Space Weather Prediction Center and available from <https://github.com/NOAA-SWPC>. The Data Assimilation Research Testbed (DART) software was developed by the National Center for Atmospheric Research (NCAR) Computational and Information Systems Lab and available from <http://dart.ucar.edu>. The Thermosphere Ionosphere Electrodynamics General Circulation Model (TIEGCM) software was developed by the NCAR High Altitude Observatory and available from <http://www.hao.ucar.edu/modeling/tgcm/tie.php>. Abel inversion algorithm code was developed by the COSMIC Data Analysis and Archive Center (CDAAC) and available from <https://cdaac-www.cosmic.ucar.edu/>.

The Observing System Simulation Experiment data used for the experiment ensembles, control, and nature runs used in this study are available at [https://osf.io/em7fk/?view\\_only=309c10ed65d34ea8920ca1281d570a76](https://osf.io/em7fk/?view_only=309c10ed65d34ea8920ca1281d570a76) via <https://doi.org/10.17605/OSF.IO/EM7FK> with open source access.

## Acknowledgments

This work was supported by the National Ocean and Atmospheric Administration (NOAA) Office of Space Weather Observations (SWO), through the UCAR subaward SUBAWD00003038, as well as the NSF award AGS 1848544 (CAREER) and the NASA award 80NSSC23K1631 (FINESST) to the University of Colorado Boulder. Chi-Yen Lin and Charles Lin are partly supported by Taiwan Space Agency under TASA-S-1120747. The authors thank Irfan Azeem and Dimitrios Vassiliadis at the NOAA SWO for their guidance and feedback on the project. The authors would like to acknowledge high-performance computing support from Cheyenne (doi:10.5065/D6RX99HX) provided by NSF NCAR's Computational and Information Systems Laboratory, sponsored by the National Science Foundation.

## References

- Akmaev, R. A. (2011). Whole atmosphere modeling: Connecting terrestrial and space weather. *Reviews of Geophysics*, *49*(4).
- Anderson, J. L. (2001). An ensemble adjustment Kalman filter for data assimilation. *Monthly weather review*, *129*(12), 2884–2903. doi: 10.1175/1520-0493(2001)129<2884:AEAKFF>2.0.CO;2
- Anderson, J. L., Hoar, T., Raeder, K., Liu, H., Collins, N., Torn, R., & Avellano, A. (2009). The data assimilation research testbed: A community facility. *Bulletin of the American Meteorological Society*, *90*(9), 1283–1296. doi: 10.1175/2009BAMS2618.1
- Andersson, E., & Masutani, M. (2010). Collaboration on observing system simulation experiments (Joint OSSE). *ECMWF Newsletter*, *123*, 14–16.
- Angling, M. J., Nogués-Correig, O., Nguyen, V., Vetra-Carvalho, S., Bocquet, F. X., Nordstrom, K., ... Masters, D. (2021). Sensing the ionosphere with the Spire radio occultation constellation. *Journal of Space Weather and Space Climate*, *11*(2001). doi: 10.1051/swsc/2021040
- Anthes, R. A., Bernhardt, P. A., Chen, Y., Cucurull, L., Dymond, K. F., Ector, D., ... Others (2008). The COSMIC/FORMOSAT-3 mission: Early results. *Bulletin of the American Meteorological Society*, *89*(3), 313–334. doi: 10.1175/BAMS-89-3-313
- Anthes, R. A., Hui Shao, Christian Marquardt, & Benjamin Ruston. (2023). *Radio Occultation Modeling Experiment (ROMEX) Framework*. Retrieved from <https://irowg.org/ro-modeling-experiment-romex/#>
- Chartier, A. T., Jackson, D. R., & Mitchell, C. N. (2013). A comparison of the

- 673 effects of initializing different thermosphere- ionosphere model fields on storm  
674 time plasma density forecasts. *Journal of Geophysical Research: Space Physics*,  
675 *118*(11), 7329–7337. doi: 10.1002/2013JA019034
- 676 Cherniak, I., Zakharenkova, I., Braun, J., Wu, Q., Pedatella, N., Schreiner, W.,  
677 ... Hunt, D. (2021). Accuracy assessment of the quiet-time ionospheric F2  
678 peak parameters as derived from COSMIC-2 multi-GNSS radio occultation  
679 measurements. *Journal of Space Weather and Space Climate*, *11*, 1–14. doi:  
680 10.1051/swsc/2020080
- 681 Chou, M. Y., Lin, C. C., Tsai, H. F., & Lin, C. Y. (2017). Ionospheric electron den-  
682 sity inversion for Global Navigation Satellite Systems radio occultation using  
683 aided Abel inversions. *Journal of Geophysical Research: Space Physics*, *122*(1),  
684 1386–1399. doi: 10.1002/2016JA023027
- 685 Dietrich, N., Matsuo, T., & Hsu, C.-T. (2022). Specifying Satellite Drag Through  
686 Coupled Thermosphere-Ionosphere Data Assimilation of Radio Occultation  
687 Electron Density Profiles. *Space Weather*, *20*. Retrieved from [https://](https://agupubs.onlinelibrary.wiley.com/doi/abs/10.1029/2022SW003147)  
688 [agupubs.onlinelibrary.wiley.com/doi/abs/10.1029/2022SW003147](https://doi.org/10.1029/2022SW003147) doi:  
689 <https://doi.org/10.1029/2022SW003147>
- 690 Errico, R. M., Yang, R., Privé, N. C., Tai, K.-S., Todling, R., Sienkiewicz, M. E., &  
691 Guo, J. (2013). Development and validation of observing-system simulation  
692 experiments at NASA’s Global Modeling and Assimilation Office. *Quarterly*  
693 *Journal of the Royal Meteorological Society*, *139*(674), 1162–1178.
- 694 Fong, C. J., Chu, C. H., Lin, C. L., & Curiel, A. D. S. (2019). Toward the Most  
695 Accurate Thermometer in Space: FORMOSAT-7/COSMIC-2 Constella-  
696 tion. *IEEE Aerospace and Electronic Systems Magazine*, *34*(8), 12–20. doi:  
697 10.1109/MAES.2019.2924133
- 698 Forsythe, V. V., Azeem, I., Blay, R., Crowley, G., Gasperini, F., Hughes, J., ...  
699 Wu, W. (2021). Evaluation of the New Background Covariance Model  
700 for the Ionospheric Data Assimilation. *Radio Science*, *56*(8), 1–10. doi:  
701 10.1029/2021RS007286
- 702 Forsythe, V. V., Azeem, I., & Crowley, G. (2020). Ionospheric Horizontal Correla-  
703 tion Distances: Estimation, Analysis, and Implications for Ionospheric Data  
704 Assimilation. *Radio Science*, *55*(12), 1–14. doi: 10.1029/2020RS007159
- 705 Gaspari, G., & Cohn, S. E. (1999). Construction of correlation functions in two  
706 and three dimensions. *Quarterly Journal of the Royal Meteorological Society*,  
707 *125*(554), 723–757. doi: 10.1256/smsqj.55416
- 708 Hajj, G. A., & Romans, L. J. (1998). Ionospheric electron density profiles obtained  
709 with the Global Positioning System: Results from the GPS/MET experiment.  
710 *Radio Science*, *33*(1), 175–190.
- 711 He, J., Yue, X., Wang, W., & Wan, W. (2019). EnKF Ionosphere and Thermo-  
712 sphere Data Assimilation Algorithm Through a Sparse Matrix Method. *Jour-  
713 nal of Geophysical Research: Space Physics*, *124*(8), 7356–7365. doi: 10.1029/  
714 2019JA026554
- 715 Hoffman, R. N., & Atlas, R. (2016). Future observing system simulation experi-  
716 ments. *Bulletin of the American Meteorological Society*, *97*(9), 1601–1616.
- 717 Hsu, C. T., Matsuo, T., & Liu, J. Y. (2018). Impact of Assimilating the  
718 FORMOSAT-3/COSMIC and FORMOSAT-7/COSMIC-2 RO Data on the  
719 Midlatitude and Low-Latitude Ionospheric Specification. *Earth and Space*  
720 *Science*, *5*(12), 875–890. doi: 10.1029/2018EA000447
- 721 Hsu, C.-T., Matsuo, T., Wang, W., & Liu, J.-Y. (2014). Effects of inferring  
722 unobserved thermospheric and ionospheric state variables by using an En-  
723 semble Kalman Filter on global ionospheric specification and forecasting.  
724 *Journal of Geophysical Research: Space Physics*, *119*(11), 9256–9267. doi:  
725 10.1002/2014JA020390
- 726 Jee, G., Burns, A. G., Wang, W., Solomon, S. C., Schunk, R. W., Scherliess, L., ...  
727 Zhu, L. (2007). Duration of an ionospheric data assimilation initialization of

- 728 a coupled thermosphere-ionosphere model. *Space Weather*, 5(1), 1–11. doi:  
729 10.1029/2006SW000250
- 730 Kelley, M. C., Wong, V. K., Aponte, N., Coker, C., Mannucci, A. J., & Komjathy,  
731 A. (2009). Comparison of COSMIC occultation-based electron density pro-  
732 files and TIP observations with Arecibo incoherent scatter radar data. *Radio*  
733 *Science*, 44(4), n/a–n/a. doi: 10.1029/2008rs004087
- 734 Kursinski, E. R., Hajj, G. A., Schofield, J. T., Linfield, R. P., & Hardy, K. R.  
735 (1997). Observing Earth’s atmosphere with radio occultation measurements  
736 using the global positioning system. *Journal of Geophysical Research Atmo-*  
737 *spheres*, 102(19), 23429–23465. doi: 10.1029/97jd01569
- 738 Lee, I. T., Matsuo, T., Richmond, A. D., Liu, J. Y., Wang, W., Lin, C. H., ...  
739 Chen, M. Q. (2012). Assimilation of FORMOSAT-3/COSMIC electron density  
740 profiles into a coupled thermosphere/ionosphere model using ensemble Kalman  
741 filtering. *Journal of Geophysical Research: Space Physics*, 117(10), 1–11. doi:  
742 10.1029/2012JA017700
- 743 Lee, I. T., Tsai, H. F., Liu, J. Y., Lin, C. H., Matsuo, T., & Chang, L. C. (2013).  
744 Modeling impact of FORMOSAT-7/COSMIC-2 mission on ionospheric space  
745 weather monitoring. *Journal of Geophysical Research: Space Physics*, 118(10),  
746 6518–6523. doi: 10.1002/jgra.50538
- 747 Lei, J., Syndergaard, S., Burns, A. G., Solomon, S. C., Wang, W., Zeng, Z., ... Lin,  
748 C. H. (2007). Comparison of COSMIC ionospheric measurements with ground-  
749 based observations and model predictions: Preliminary results. *Journal of Geo-*  
750 *physical Research: Space Physics*, 112(7), 1–10. doi: 10.1029/2006JA012240
- 751 Lin, C. Y., Lin, C. C. H., Liu, J. Y., Rajesh, P. K., Matsuo, T., Chou, M. Y., ...  
752 Yeh, W. H. (2020). The Early Results and Validation of FORMOSAT-  
753 7/COSMIC-2 Space Weather Products: Global Ionospheric Specification and  
754 Ne-Aided Abel Electron Density Profile. *Journal of Geophysical Research:*  
755 *Space Physics*, 125(10), 1–12. doi: 10.1029/2020JA028028
- 756 Lin, C. Y., Matsuo, T., Liu, J. Y., Lin, C. H., Huba, J. D., Tsai, H. F., & Chen,  
757 C. Y. (2017). Data Assimilation of Ground-Based GPS and Radio Occulta-  
758 tion Total Electron Content for Global Ionospheric Specification. *Journal of*  
759 *Geophysical Research: Space Physics*, 122(10), 10,810–876,886. Retrieved  
760 from [https://agupubs.onlinelibrary.wiley.com/doi/abs/10.1002/](https://agupubs.onlinelibrary.wiley.com/doi/abs/10.1002/2017JA024185)  
761 [2017JA024185](https://doi.org/10.1002/2017JA024185) doi: <https://doi.org/10.1002/2017JA024185>
- 762 Lin, C. Y., Matsuo, T., Liu, J. Y., Lin, C. H., Tsai, H. F., & Araujo-Pradere, E. A.  
763 (2015). Ionospheric assimilation of radio occultation and ground-based GPS  
764 data using non-stationary background model error covariance. *Atmospheric*  
765 *Measurement Techniques*, 8(1), 171–182. doi: 10.5194/amt-8-171-2015
- 766 Liu, J. Y., Lin, C. Y., Lin, C. H., Tsai, H. F., Solomon, S. C., Sun, Y. Y., ...  
767 Kuo, Y. H. (2010). Artificial plasma cave in the low-latitude iono-  
768 sphere results from the radio occultation inversion of the FORMOSAT-  
769 3/COSMIC. *Journal of Geophysical Research: Space Physics*, 115(7), 1–8.  
770 doi: 10.1029/2009JA015079
- 771 Lugaz, N. (2020). PROSWIFT Bill and the 2020 Space Weather Operations and  
772 Research Infrastructure Workshop From the National Academies of Sciences,  
773 Engineering, and Medicine. *Space Weather*, 18(10), e2020SW002628. Retrieved  
774 from [https://agupubs.onlinelibrary.wiley.com/doi/abs/10.1029/](https://agupubs.onlinelibrary.wiley.com/doi/abs/10.1029/2020SW002628)  
775 [2020SW002628](https://doi.org/10.1029/2020SW002628) doi: <https://doi.org/10.1029/2020SW002628>
- 776 Maruyama, N., Sun, Y.-Y., Richards, P. G., Middlecoff, J., Fang, T.-W., Fuller-  
777 Rowell, T. J., ... Valladares, C. E. (2016). A new source of the midlatitude  
778 ionospheric peak density structure revealed by a new Ionosphere-Plasmasphere  
779 model. *Geophysical Research Letters*, 43(6), 2429–2435.
- 780 Masutani, M., Andersson, E., Terry, J., Reale, O., Jusem, J. C., Riishojgaard, L. P.,  
781 ... Others (2007). Progress in Joint OSSEs A new nature run and inter-  
782 national collaboration. In *Proceedings of the 12th conference on integrated*

- 783 *observing and assimilation systems for atmospheres, oceans, and land surface*  
784 *(ioas-aols).*
- 785 Matsuo, T., & Hsu, C.-T. (2021). Inference of Hidden States by Coupled  
786 Thermosphere-Ionosphere Data Assimilation: Applications to Observability  
787 and Predictability of Neutral Mass Density. *Upper Atmosphere Dynamics and*  
788 *Energetics*, 343–363. doi: 10.1002/9781119815631.ch18
- 789 Moreno, B., Radicella, S., De Lacy, M. C., Herraiz, M., & Rodriguez-Caderot, G.  
790 (2011). On the effects of the ionospheric disturbances on precise point posi-  
791 tioning at equatorial latitudes. *GPS solutions*, 15, 381–390.
- 792 Pedatella, N. M., Anderson, J. L., Chen, C. H., Raeder, K., Liu, J., Liu, H. L., &  
793 Lin, C. H. (2020). Assimilation of Ionosphere Observations in the Whole  
794 Atmosphere Community Climate Model with Thermosphere-Ionosphere EX-  
795 tension (WACCMX). *Journal of Geophysical Research: Space Physics*, 125(9),  
796 1–15. doi: 10.1029/2020JA028251
- 797 Pedatella, N. M., Yue, X., & Schreiner, W. S. (2015). An improved inversion for  
798 FORMOSAT-3 / COSMIC. *Journal of Geophysical Research : Space Physics*,  
799 8942–8953. doi: 10.1002/2015JA021704.Received
- 800 Qian, L., Burns, A. G., Emery, B. A., Foster, B., Lu, G., Maute, A., ... Wang, W.  
801 (2014). The NCAR TIE-GCM: A community model of the coupled thermo-  
802 sphere/ionosphere system. *Modeling the ionosphere-thermosphere system*, 201,  
803 73–83. doi: 10.1029/2012GM001297
- 804 Richmond, A. D., Ridley, E. C., & Roble, R. G. (1992). A thermosphere/ionosphere  
805 general circulation model with coupled electrodynamics. *Geophysical Research*  
806 *Letters*, 19(6), 601–604. doi: 10.1029/92GL00401
- 807 Scherliess, L., Schunk, R. W., Sojka, J. J., & Thompson, D. C. (2004). Develop-  
808 ment of a physics-based reduced state Kalman filter for the ionosphere. *Radio*  
809 *Science*, 39(1), 231–242. doi: 10.1029/2002rs002797
- 810 Schreiner, W. S., Sokolovskiy, S. V., Rocken, C., & Hunt, D. C. (1999). Analysis and  
811 validation of GPS/MET radio occultation data in the ionosphere. *Radio Sci-*  
812 *ence*, 34(4), 949–966.
- 813 Tsai, L. C., Liu, J. Y., Schreiner, W. S., & Berkey, F. T. (2001). Comparisons of  
814 GPS/MET retrieved ionospheric electron density and ground based ionosonde  
815 data. *Earth, Planets and Space*, 53(3), 193–205. doi: 10.1186/BF03352376
- 816 Tsai, L. C., & Tsai, W. H. (2004). Improvement of GPS/MET ionospheric profil-  
817 ing and validation using the Chung-Li ionosonde measurements and the IRI  
818 model. *Terrestrial, Atmospheric and Oceanic Sciences*, 15(4), 589–607. doi:  
819 10.3319/TAO.2004.15.4.589(A)
- 820 Tulasi Ram, S., Su, S. Y., Tsai, L. C., & Liu, C. H. (2016). A self-contained  
821 GIM-aided Abel retrieval method to improve GNSS-Radio Occultation re-  
822 trieved electron density profiles. *GPS Solutions*, 20(4), 825–836. doi:  
823 10.1007/s10291-015-0491-z
- 824 Vourlidas, A., Turner, D., Biesecker, D., Coster, A., Engell, A., Ho, G., ... Spann,  
825 J. (2023). The NASA space weather science and observation gap analysis. *Ad-*  
826 *vances in Space Research*. Retrieved from [https://www.sciencedirect.com/](https://www.sciencedirect.com/science/article/pii/S0273117723005057)  
827 [science/article/pii/S0273117723005057](https://www.sciencedirect.com/science/article/pii/S0273117723005057) doi: [https://doi.org/10.1016/](https://doi.org/10.1016/j.asr.2023.06.046)  
828 [j.asr.2023.06.046](https://doi.org/10.1016/j.asr.2023.06.046)
- 829 Wu, D. L. (2018). New global electron density observations from GPS-RO in the  
830 D- and E-Region ionosphere. *Journal of Atmospheric and Solar-Terrestrial*  
831 *Physics*, 171, 36–59. Retrieved from [https://www.sciencedirect.com/](https://www.sciencedirect.com/science/article/pii/S1364682617301050)  
832 [science/article/pii/S1364682617301050](https://www.sciencedirect.com/science/article/pii/S1364682617301050) doi: [https://doi.org/10.1016/](https://doi.org/10.1016/j.jastp.2017.07.013)  
833 [j.jastp.2017.07.013](https://doi.org/10.1016/j.jastp.2017.07.013)
- 834 Yue, X., Schreiner, W. S., & Kuo, Y.-H. (2013). Evaluating the effect of the global  
835 ionospheric map on aiding retrieval of radio occultation electron density pro-  
836 files. *GPS solutions*, 17, 327–335.
- 837 Yue, X., Schreiner, W. S., Kuo, Y. H., Braun, J. J., Lin, Y. C., & Wan, W. (2014).

- 838 Observing system simulation experiment study on imaging the ionosphere by  
839 assimilating observations from ground GNSS, LEO-based radio occultation and  
840 ocean reflection, and cross link. *IEEE Transactions on Geoscience and Remote  
841 Sensing*, 52(7), 3759–3773. doi: 10.1109/TGRS.2013.2275753
- 842 Yue, X., Schreiner, W. S., Lei, J., Sokolovskiy, S. V., Rocken, C., Hunt, D. C., &  
843 Kuo, Y. H. (2010). Error analysis of Abel retrieved electron density profiles  
844 from radio occultation measurements. *Annales Geophysicae*, 28(1), 217–222.  
845 doi: 10.5194/angeo-28-217-2010
- 846 Yue, X., Schreiner, W. S., Pedatella, N., Anthes, R. A., Mannucci, A. J., Straus,  
847 P. R., & Liu, J. Y. (2014). Space weather observations by GNSS radio occul-  
848 tation: From FORMOSAT-3/COSMIC to FORMOSAT-7/COSMIC-2. *Space  
849 Weather*, 12(11), 616–621. doi: 10.1002/2014SW001133
- 850 Zhang, S., Wu, X., & Hu, X. (2023). Ionospheric Vertical Correlation Distance  
851 Calculation Based on COSMIC Electron Density Profile Data. *Journal of  
852 Geophysical Research: Space Physics*, 128(7), e2023JA031453. Retrieved  
853 from [https://agupubs.onlinelibrary.wiley.com/doi/abs/10.1029/  
854 2023JA031453](https://agupubs.onlinelibrary.wiley.com/doi/abs/10.1029/2023JA031453) doi: <https://doi.org/10.1029/2023JA031453>